Subsurface microstructural changes in a cast heat resisting alloy caused by high temperature corrosion

D. Oquab [1], N. Xu [2], D. Monceau [1], D.J. Young *

School of Materials Science and Engineering, University of New South Wales, Sydney, NSW 2052, Australia

A B S T R A C T

A cast HP ModNb alloy (Fe–25Cr–35Ni–1Nb, wt.%) was oxidised and carburised in CO–CO_2 corresponding to $a_C = 0.1$ and $p_{O_2} = 3 \times 10^{-16}$ atm at 1080 °C. Formation of an external, chromium-rich oxide scale led to depletion of this metal in a deep alloy subsurface zone. Within that zone, secondary chromium-rich carbides dissolved, primary carbides oxidised, solute silicon and aluminium internally oxidised, and extensive porosity developed. Pore volumes correspond to the difference between metal loss by scaling and metal displacement by internal oxidation, assuming the scale–metal interface to be fixed. The pores are concluded to be Kirkendall voids.

Keywords:
A. Alloy
C. High temperature corrosion
C. Carburization
C. Internal oxidation

1. Introduction

Heat resisting steels and nickel–base alloys are centrifugally cast as tubes for service in high temperature chemical processes such as steam reforming and hydrocarbon cracking. Alloy microstructures consist mainly of austenite dendrites and primary, interdendritic, chromium-rich carbide, $M_{23}C_6$. In the case of niobium-modified compositions, NbC is also present. Depending on their thermal history, the alloys may also contain fine, secondary chromium-rich carbides within the austenite. A typical commercial alloy composition is given in Table 1, and its microstructure is shown in Fig. 1. This alloy has a composition meeting the HP40Nb specification.

During service, these alloys are exposed to hot process gases which are mildly oxidising and strongly carburising. Corrosion resistance is achieved by the development of a chromia scale, which grows slowly and acts as a barrier to carbon ingress. The performance of this scale is enhanced by the development beneath it of a semi-continuous layer of silica [1–5]. Selective oxidation of chromium results in the development of a subsurface depletion zone in which prior carbides are either dissolved or oxidised in situ [1–5]. Eventually, depletion becomes so severe that internal carburisation of the alloy commences and subsequent alloy damage results. An overall view of the reaction morphology is shown in Fig. 2.

Corresponding author. Tel.: +61 2 9385 4322; fax: +61 2 9385 5956.
E-mail addresses: d.young@unsw.edu.au, s7801712@unsw.edu.au (D.J. Young).
[1] Permanent address: CIRIMAT, ENSIACET(INPT), 31077 Toulouse, France.
[2] Present address: HRL Technology Pty Ltd, 677 Springvale Rd., Mulgrave, Vic. 3170, Australia.

Characterising the development of alloy subsurface microstructures is important to an understanding of how to optimise alloy design or selection. In addition to carbide dissolution and oxidation, internal silicon and aluminium oxides precipitate within the affected zone [6–9]. A consideration of the volume changes associated with these various events shows [8] that the volume of metal consumed by scale growth exceeds the volume change associated with internal oxidation, but the way in which the net volume loss is accommodated has never been established.

This paper describes a microstructural investigation of the subsurface depletion zone developed by a cast heat resisting alloy during exposure to an oxidising–carburising gas.

2. Experimental

The commercial heat resisting steel specified in Table 1 was used. Rectangular alloy samples ($10 \times 5 \times 2$ mm) were cut from the walls of a centrifugally cast tube, with their principal surfaces normal to the tube axis. Sample surfaces were ground to a 600 grit finish and ultrasonically cleaned in acetone immediately before use.

The alloy was exposed at 1080 °C to a flowing 95.7% CO–4.3% CO_2 gas mixture at a total pressure close to 1 atm. Gas compositions were regulated using mass flow controllers, and were calculated to yield an equilibrium carbon activity of 0.1 and oxygen partial pressure of 3×10^{-16} atm. The potentials realised are similar to those in effect in overheated steam reformers at a total pressure of about 30 atm. The alloy was reacted for 1000 h.

Reacted samples were characterised using conventional metallographic techniques. In addition, a series of transmission electron

Table 1
Alloy compositions (wt.%) with balance Fe.

	Ni	Cr	Nb	Si	Al	Ta	Mo	Mn	W	Ti	C	S
HP40Nb	33–37	24–28		2.5 max			0.5 max	2.0 max			0.35–0.75	0.04 max
Test alloy	34.9	26.0	1.4	0.6	560*	0.2	0.1	0.7	1.0	0.14	0.41	0.006

* Units of ppm.

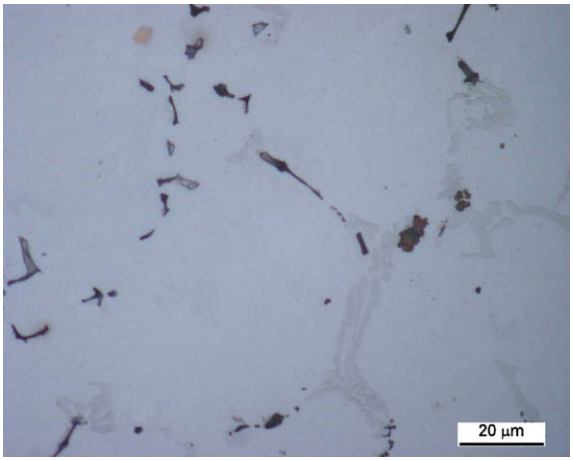

Fig. 1. Microstructure of as-received cast alloy.

microscope (TEM) foils was prepared by focused ion beam (FIB) milling. FIB foil preparation was performed using an FEI Noava Nanolab 200 Dual-Beam™ system. TEM analysis was carried out using a JEOL JEM 2010 electron microscope equipped with a TRACOR EDX system.

3. Results and discussion

Metallographic cross-sections of the alloy subsurface region after reaction are shown in Fig. 2. Similar structures were also seen after only 100 h reaction [9]. The external scale consists [9] of an outer layer of $MnCr_2O_4$ and a thicker, inner layer of Cr_2O_3. This is the usual scale constitution developed by heat resisting steels [1–3], and reflects their high chromium concentrations and the rapid diffusion of manganese in Cr_2O_3 [10]. This selective oxidation of chromium is accompanied by subsurface alloy depletion, made evident in this region (Fig. 2) by the disappearance of secondary carbides. Internal oxidation has also occurred within the affected subsurface region, and internal carburisation deeper within the alloy. Large amounts of silica formed an almost continuous band in some areas (Fig 2a), but discrete precipitates in others (Fig 2b). The oxidation of interdendritic carbides [3,5,8] and the internal carburisation processes [9,11,12] are discussed elsewhere. Attention is directed here to the microstructural changes occurring within the austenite matrix of the subsurface alloy.

Fig. 3 shows an SEM image of the affected alloy zone cross-section, from which a series of TEM foil samples were FIB milled. The depths beneath the alloy–scale interface of the different milling location mid-points are listed in Table 2.

3.1. Intragranular oxide precipitates

Multiple, very fine precipitates are seen in Fig. 4 to have formed immediately beneath the alloy–scale interface. These were identified by EDX analysis as oxides, variously rich in Si, Al, Nb + Cr + Al, Ti + Al + Cr, and all of Al + Cr + Ti + Nb. It is possible that the chemically complex oxides were in fact agglomerations of simpler oxide precipitates. Thus all alloy components apart from the solvent iron and nickel had undergone internal oxidation. The silica precipitate was identified by its diffraction pattern as tetragonal cristobalite (Fig. 5) and the alumina was either the θ- or the γ-phase.

Small oxide precipitates of many solute metals were also found somewhat deeper within the depleted zone, at position 2 in Fig. 3. However, still deeper, at position 4, silica was not precipitated. Deeper still, at position 6, the precipitates were predominantly needle-shaped alumina. Fig. 6 shows a bright field image, along with a selected area diffraction pattern of the austenite matrix and of the precipitate itself. Internal oxidation was no longer evident at position 7. Instead, fine precipitates of Cr_7C_3 were found to be profusely distributed in this region (Fig. 7).

Intragranular precipitate identifications are summarised in Table 2, along with their location depths. The observed development of multiple internal precipitation zones is a consequence of the gradients in oxidant potentials, both oxygen and carbon, within the affected alloy region [13–15]. The distribution of oxide precipitates reflects local equilibrium with an oxygen potential which varies from a maximum at the alloy–scale interface to a minimum in the alloy interior. Thus only the most stable oxide, alumina, precipitates where the oxygen potential approaches its lowest value, whereas even the least stable of the oxides, chromia, is precipitated near the surface, where the oxygen potential is highest. The intermediate stability oxide, silica, is precipitated within much the same region as chromia, i.e. within about 55 µm of the surface. Although SiO_2 is more stable than Cr_2O_3, similar precipitation depths result because the alloy is much more dilute in silicon than chromium.

Finally, the development of an internal carburisation zone beneath an internal oxidation zone results from the rapid diffusion of carbon, combined with the fact that carbides are less stable than oxides. At or near the surface, where both oxygen and carbon are available, the more stable oxides are formed because reactions such as:

$$2Cr_7C_3 + \frac{21}{2}O_2 = 7Cr_2O_3 + 6C \quad (1)$$

are strongly favoured. Beneath the surface, oxygen is consumed, and its activity decreases with depth, until reaching a low value at the oxide precipitation front. However, if carbon diffusion through the near-surface oxide precipitation zone is fast, then a_C does not decrease very much, and a position is reached where a_C/a_O exceeds the value necessary to stabilise Cr_7C_3, and precipitation of the latter phase commences.

A schematic representation of elemental activity profiles is shown in Fig. 8. It is seen that internal oxidation leads to activity gradients in solute metals which tend to drive diffusion from the underlying alloy toward the subsurface region. It is this process which produces enrichment of dilute components such as aluminium and silicon, accounting for the precipitation of significant oxide volume fractions.

3.2. Subsurface porosity development

Examination of Fig. 3 reveals the development within the chromium depletion zone of numerous approximately circular

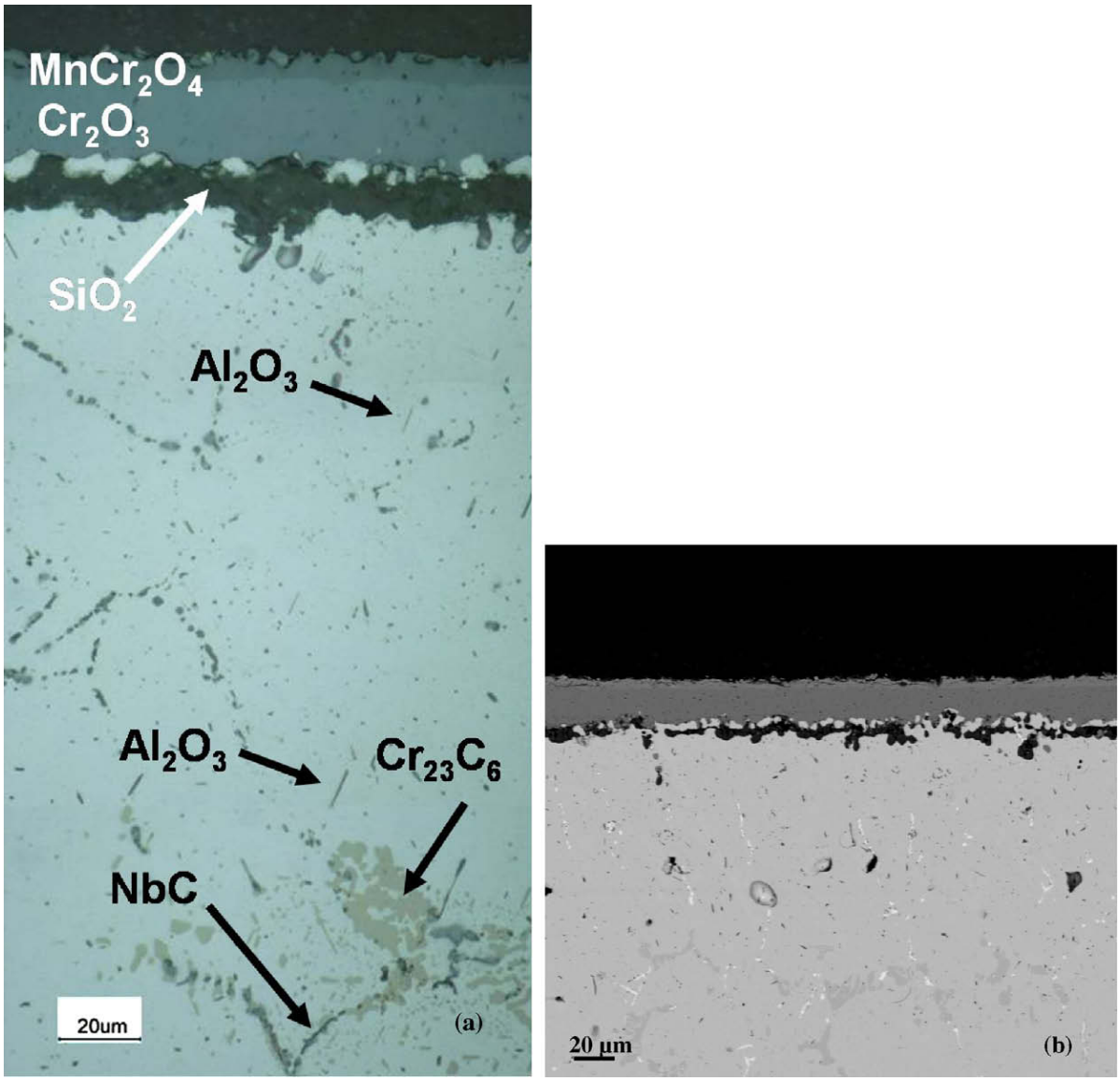

Fig. 2. Cross-sections of alloy surface after 1000 h reaction: (a) optical view, stain etched (b) back-scattered electron image.

features. Fig. 10 shows more clearly their positioning throughout the depletion zone. It is difficult to identify these objects from their appearance in a metallographic section. They could be pores, or they could result from metallographic pullout of second-phase particles. Chemical analysis shows that they contain oxides, but this material could be the result of internal oxidation reactions or it could merely be detritus collected in the specimen preparation process. This uncertainty is resolved by serial sectioning in the FIB.

A series of FIB milled sections in Fig. 9 approaches and intersects with one of the circular features seen in the metallographically prepared surface. Clearly the feature is a cavity which has material collected in its opening. Another cavity has been revealed in the lower right-hand corner of these sections, beneath the metallographically prepared surface. It is close to spherical in shape, but has a faceted surface, and contains small particles of alumina, identified by EDX analysis. This cavity or pore is obviously not an artefact of metallographic preparation, but rather a product of the corrosion and chromium depletion processes. Both the driving force for formation of pores and the way in which they nucleate are of interest.

Significant volume changes accompany the phase transformations resulting from oxidation:

$$2\underline{\mathrm{Cr}} + \frac{3}{2}\mathrm{O_2(g)} = \mathrm{Cr_2O_3(s)} \tag{2}$$

$$\mathrm{Cr_{23}C_6} + \frac{69}{2}\underline{\mathrm{O}} = \frac{23}{2}\mathrm{Cr_2O_3} + 6\underline{\mathrm{C}} \tag{3}$$

$$\underline{\mathrm{Si}} + 2\underline{\mathrm{O}} = \mathrm{SiO_2} \tag{4}$$

where underlining indicates solute species, and the large, primary interdendritic carbides are considered. Internal oxidation of the other solute species contributes much less volume change. The kinetics of the above three processes are diffusion controlled and parabolic [3,5,8,9]:

$$X^2 = k_\mathrm{p} t \tag{5}$$

$$X_{(i)}^2 = k_\mathrm{p}^{(i)} t \tag{6}$$

Here X is the scale thickness and $X_{(i)}$ the subsurface depth to which either solute silicon or interdendritic carbides are oxidised in time, t, and k_p, $k_\mathrm{p}^{(i)}$ are rate constants.

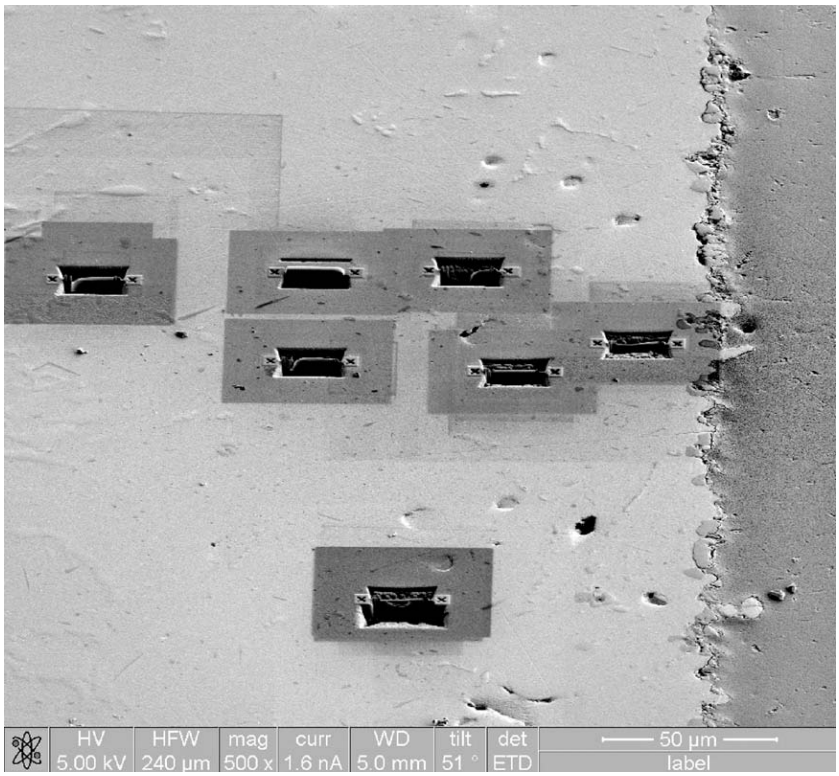

Fig. 3. FIB image of reacted alloy subsurface zone, showing where TEM foils were milled.

Table 2
FIB milling location depths* and precipitate identifications.

Location	Depth/µm	Precipitate By EDS	Identification By SAD
1	20	Si–O, Al–O, Al–Ti–Cr–O, Nb–Cr–Al–O, Ti–Al–Cr, Al–Cr–Ti–Nb	SiO_2 (cr), θ/γ-Al_2O_3
2	55	Si–O, Al–O, Al–Ti–Cr–O, Nb–Cr–Al–O, Ti–Al–Cr, Al–Cr–Ti–Nb	SiO_2 (cr), θ/γ-Al_2O_3
3	70		
4	84	Al–O, Al–Ti–Cr–O, Nb–Cr–Al–O, Ti–Al–Cr, Al–Cr–Ti–Nb	θ/γ-Al_2O_3
5, 6	113		θ/γ-Al_2O_3
7	175		Cr_7C_3

* Beneath alloy–scale interface.

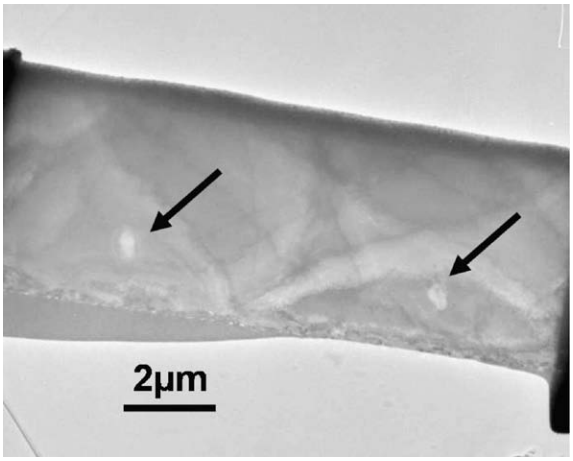

Fig. 4. TEM bright field image showing precipitates (arrowed) at position 1 in Fig. 3.

The measured extent of reaction is now used to calculate volume changes in the alloy subsurface reaction zone: volume increases due to carbide oxidation and silica precipitation, and a volume decrease due to preferential removal of chromium into the oxide scale.

Examination of the reaction morphology after 1000 h shows that $X = 25$ µm, $X_{(i)}(\mathrm{Si}) = 15$ µm and $X_{(i)}(\mathrm{Cr}) = 170$ µm. The volume change per unit sample surface area due to primary carbide oxidation, $\Delta V(\mathrm{Cr})/A$, is given by

$$\Delta V(\mathrm{Cr})/A = f_v(\mathrm{Cr}) X_{(i)}(\mathrm{Cr}) \left[\frac{V_{\mathrm{Cr_2O_3}}}{V_{\mathrm{Cr_{23}C_6}}} - 1 \right] \tag{7}$$

where $f_v(\mathrm{Cr})$ is the original carbide volume fraction and $V_{\mathrm{Cr_2O_3}}$, $V_{\mathrm{Cr_{23}C_6}}$ are the volumes of 1 mol of chromium converted into the indicated compound. Taking $V_{\mathrm{Cr_2O_3}}$ and $V_{\mathrm{Cr_{23}C_6}}$ as 14.6 and 7.91 $\mathrm{cm^3}$ per mol, respectively, and $f_v(\mathrm{Cr}) = 0.015$, the value $\Delta V(\mathrm{Cr})/A = 2.1 \times 10^{-4}$ cm is calculated. Although $V_{\mathrm{Cr_2O_3}}/V_{\mathrm{Cr_{23}C_6}}$ is large at 1.84, the overall effect is relatively small because the volume fraction of primary carbide is small.

Volume changes resulting from internal silicon oxidation are calculated from:

$$\Delta V(\mathrm{Si})/A = X_{(i)}(\mathrm{Si}) \left[f_v(\mathrm{SiO_2}) - N_{\mathrm{Si}}^{(0)} \right] \tag{8}$$

where $X_{(i)}(\mathrm{Si})$ is the depth of the silicon internal oxidation zone, $f_v(\mathrm{SiO_2})$ is the measured volume fraction of silica in the precipitation

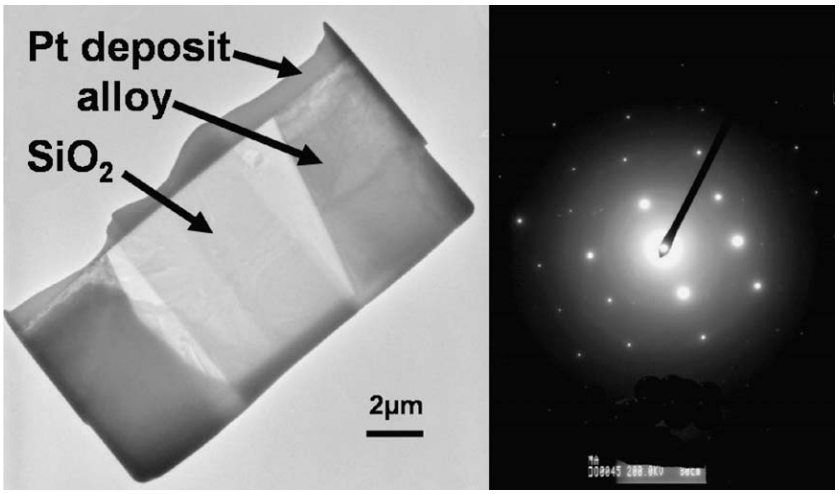

Fig. 5. TEM bright field image and SAD pattern from a near-surface cristobalite precipitate.

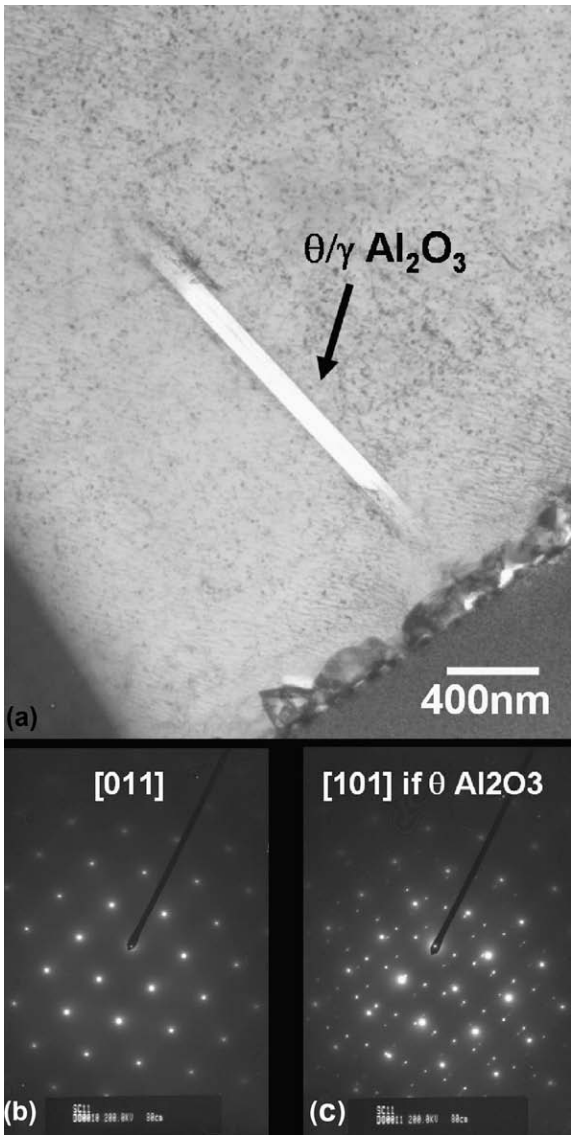

Fig. 6. Precipitate at position 6 in Fig. 3: (a) bright field image (b) SAD of austenite matrix (c) SAD of alumina precipitate.

zone, and $N_{Si}^{(0)}$ is the original alloy silicon mol fraction. Here the partial molar volume of silicon has been approximated by the alloy molar volume. The observed value of $f_v(SiO_2)$ is high at 0.31, reflecting the strong diffusional enrichment of this element [9] beneath the scale. However, the depth of the main internal silica precipitation zone is rather shallow, and a value of $\Delta V(Si) = 4.47 \times 10^{-4}$ cm is calculated.

One way in which these internal volume expansion contributions can be accommodated is by the consumption of metal in growing the external scale. Volume change within the alloy due to external scaling, $\Delta V_A/A$ per unit surface area, is calculated using the approximation that the scale is entirely Cr_2O_3, and that the alloy–scale interface is fixed. On this basis,

$$\Delta V_A/A = -X\frac{V_{Cr}}{V_{Cr_2O_3}} \tag{9}$$

and for $X = 25$ μm, it is found that $\Delta V_A/A = -1.17 \times 10^{-3}$ cm. Neglecting the very small volume change due to secondary carbide dissolution, the overall net change $\Delta V(Cr)/A + \Delta V(Si)/A + \Delta V_A/A$ is found to be -5.1×10^{-4} cm.

Clearly, if the scale–alloy interface were free to move, $\Delta V_A/A$ would be zero, and the overall net volume change per unit area is calculated as $+6.6 \times 10^{-4}$ cm. Thus the subsurface zone would be in compression rather than tension, and no driving force for void formation could thereby arise. In fact, however, the scale–alloy interface is fixed, as shown by the lack of deformation at sample corners in Fig. 11. It is concluded therefore that the conditions for the validity of (9) are met, and more than enough space to accommodate internal oxide can be made available by external growth of a rigid oxide scale. The remaining questions concern whether there is sufficiently rapid vacancy transfer within the affected zone, and whether there is sufficient excess vacancy flux to account for the void volume actually developed.

A high vacancy mobility is available, as reflected in the rapid substitutional diffusion evident within the subsurface alloy region: chromium depletion to a depth of about 170 μm, and silicon enrichment by a factor of about 20 in the internal silica precipitation zone [9]. A net flow of vacancies, which would accommodate the volume changes caused by internal oxidation, represents a difference between outward fluxes of Cr plus Si, and inward fluxes of Fe plus Ni. In the usual situation of alloy interdiffusion, such a case of unbalanced material flows is recognised as the Kirkendall effect [16]. If the alloy lattice is free to move, it will drift at a rate, v, to compensate for the different self-diffusion coefficients of the individual metals. For a binary alloy AB:

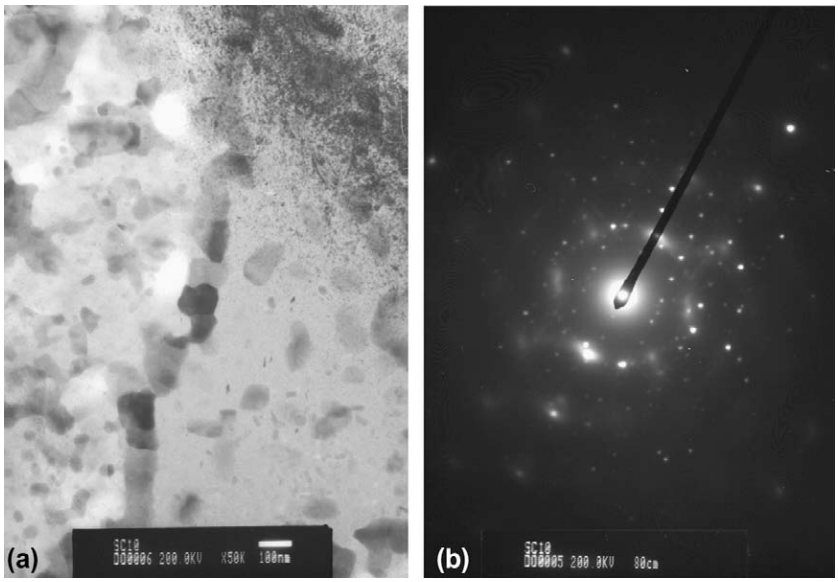

Fig. 7. Precipitates at position 7: (a) TEM bright field image (b) SAD pattern identifying grey particles in (a) as Cr_7C_3.

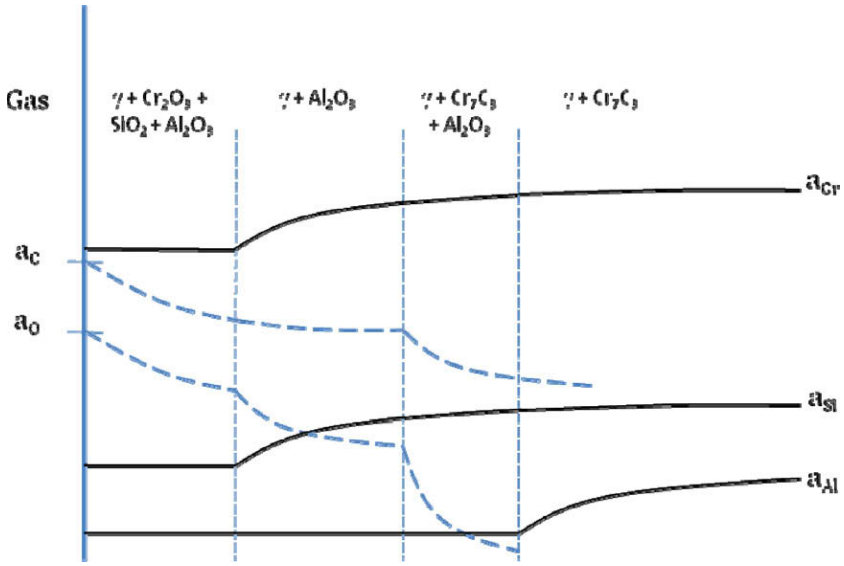

Fig. 8. Schematic view of component diffusion profiles in subsurface reaction zone.

$$v = V_{AB}(D_A - D_B)\frac{\partial C_A}{\partial x} \tag{10}$$

where V_{AB} is the alloy molar volume, D_i the self-diffusion coefficient of the indicated species and C_A the concentration. However, if the alloy is anchored to an almost rigid oxide scale, it is not free to move, and a vacancy flux results. The implied lack of deformation is evident at sample corners, as seen in Fig. 11. It is possible that the near-surface silica contributed to the rigidity of the system.

Although the volume change calculations given here are approximate, they indicate the possibility of surplus vacancy injection. Vacancies not consumed in the internal oxidation processes can condense to form the voids observed throughout the chromium depletion region. The net loss of metal volume calculated above is equivalent to a pore volume fraction, $f_v(P) = 0.09$ in an affected zone 170 μm deep. Direct measurement from Fig. 10 yields the average value $f_v(P) = 0.05$. This good agreement indicates that the observed pores are in fact Kirkendall voids.

The distribution of pores within the affected zone, and their varying sizes reflect the outcomes of the detailed nucleation and growth processes. A proper understanding of pore growth requires knowledge of the diffusion profiles (and diffusion coefficient cross-terms) within the metal matrix throughout the reaction zone, and these are not available. However, it can be observed that pores reach limited sizes. Thus the pores nearest the metal surface are presumably the oldest, but are smaller than those in the middle of the zone. Given that the pores are faceted spheres, it is reasonable to suppose that their optimum sizes are controlled by, among other things, their surface energies. The surface energy of the near-surface pores was such that their enlargement was not possible, and instead the vacancy flux swept past them to nucleate and grow new pores at greater depths. Variable pore size might be an indication of the dependence of surface tension on austenite composition. Pore nucleation is obviously not homogeneous. Instead, interfaces and boundaries provide energetically favourable nucleation sites.

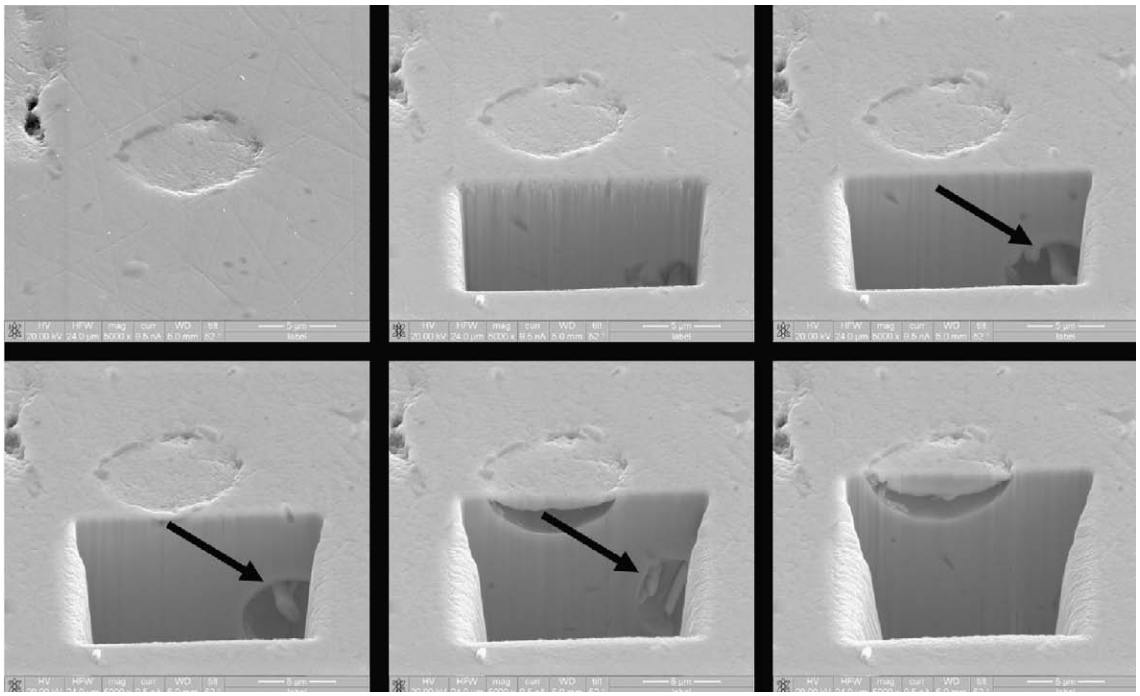

Fig. 9. Series of FIB milled sections showing that circular features are spherical cavities. Particles within cavities (arrowed) identified by EDX as alumina.

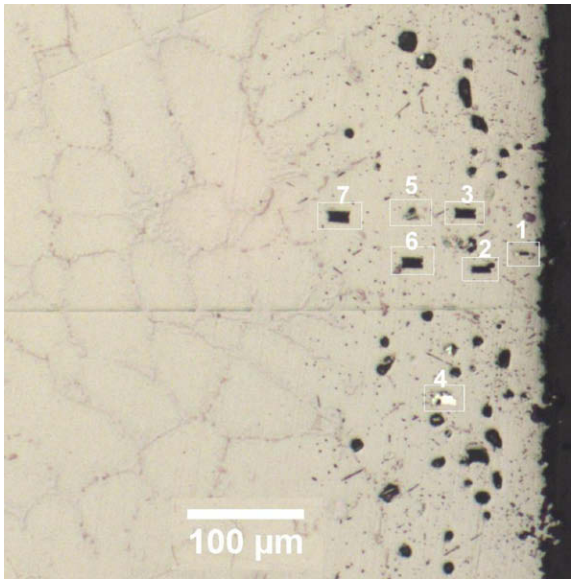

Fig. 10. Metallographic cross-section polished to show pores. Numbered rectangles are FIB milled trenches.

Clearly, the chromia scale–alloy interface did not nucleate pores resulting from vacancy condensation. The observation of small alumina precipitates within the voids suggests that oxide–matrix interfaces provided the original nucleation sites for vacancy condensation. As has been seen, only alumina is precipitated within the alloy at greater depths than those at which pores form. Thus only alumina–austenite and carbide–austenite interfaces are available as nucleation sites where voids first form. Evidently dissolution is the favoured process at secondary carbide surfaces. Although the oxidation process (3) occurs at primary carbide surfaces, either they or the stable alumina–austenite interfaces might provide sites for nucleation.

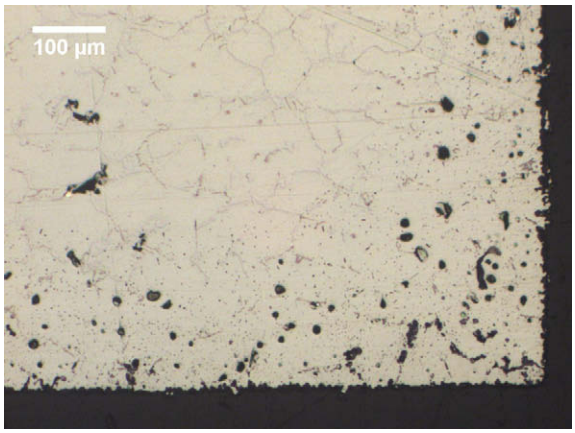

Fig. 11. Metallographic cross-section polished to show conservation of square edge at sample.

4. Summary and conclusions

Large scale microstructural changes developed in the subsurface zone of oxidised–carburised alloy: secondary carbide dissolution, primary carbide oxidation, internal oxidation of solute silicon and aluminium, and carburisation deeper within the alloy. Simultaneously, extensive porosity developed in the reaction affected zone.

It is concluded that preferential external oxidation of chromium led to its extensive depletion within the alloy, a process which drove secondary chromium carbide dissolution. Simultaneously, inward diffusion of dissolved oxygen and carbon led to internal oxidation and carburisation. These processes were supported by substitutional alloy diffusion. It is concluded from the observations of deep chromium depletion and the very large extent of silicon enrichment near the alloy surface, that alloy diffusion was rapid.

An evaluation of the volume changes accompanying the different phase changes showed that the consumption of metal by

external scaling closely matched the volume required to accommodate the internal oxidation and void formation processes. It is concluded that vacancy diffusion allowed this interchange, and that the pores were Kirkendall voids. Thus the large outward flux of chromium exceeded the reverse flux of iron and nickel, the difference providing the required vacancy flow. Void nucleation occurred preferentially at internal precipitate–austenite interfaces, but not at the chromia scale–alloy interface.

Acknowledgements

This work was supported by a French-Australian Science and Technology exchange program (project FAST 10427XF) and a grant from NANO-MNRF. In addition, the authors thank Dr Damien McGrouther (Electron Microscope Unit, UNSW), for his kind help with TEM sample preparation and Mrs. Marie-Christine Lafont (CIRIMAT Toulouse) for her help with TEM observations and analysis.

References

[1] A.DeS. Brasunas, J.T. Gow, O.E. Harder, Proc. ASTM 46 (1966) 870.
[2] K. Ledgeff, A. Rahmel, M. Schorr, Werkst. Korros. 30 (1976) 767.
[3] D.J. Young, High Temp. Technol. 1 (1982) 101.
[4] D.J. Baxter, R.T. Derricott, R.C. Hurst, Werkst. Korros. 34 (1983) 446.
[5] P. Becker, M. Panasko, D.J. Young, Oxid. Met. 64 (2005) 281.
[6] M.J. Bennett, J.B. Price, J. Mater. Sci. 16 (1981) 170.
[7] R.H. Kane, in: CORROSION 83, NACE Houston, TX, paper 266.
[8] N. Belen, P. Tomaszewicz, D.J. Young, Oxid. Met. 22 (1984) 227.
[9] N. Xu, D. Monceau, D.J. Young, J. Furtado, Corros. Sci. 50 (2008) 2398.
[10] R.E. Lobnig, H.P. Schmidt, H.J. Grabke, Oxid. Met. 37 (1992) 81.
[11] G.M. Smith, D.J. Young, D.L. Trimm, Oxid. Met. 18 (1982) 229–243.
[12] D.R.G. Mitchell, D.J. Young, W. Kleeman, Mater. Corros. 49 (1998) 231–236.
[13] J.L. Meijering, in: H. Herman (Ed.), Advances in Materials Research, Wiley-Interscience, New York, 1971, p. 1.
[14] D.J. Young, S. Watson, Oxid. Met. 44 (1995) 239.
[15] D.J. Young, High Temperature Oxidation and Corrosion of Metals, Elsevier, Amsterdam, 2008.
[16] A. Smigelskas, E. Kirkendall, Trans. AIME 171 (1947) 130.